physica status solidi rrl
www.pss-rapid.com

Novel 2D PC_5 with a Dirac Cone and Edge-Size Dependence

Ling Shang, Peng-Fei Liu, Heng Gao, Wei Wu, Yin Wang, Zhibin Gao, Bao-Tian Wang, and Wei Ren**

2D materials with Dirac cones, which show a linear band character near the Fermi level, exhibit many novel properties. Herein, based on first-principles calculations, the 2D phosphorus carbide (PC_5) monolayer is studied systematically. The stability is examined by calculating the formation energy, phonon dispersion, and elastic constants as well as by performing ab initio molecular dynamics (AIMD) simulations. Due to the similarity of its structure to that of graphene, one Dirac cone is exactly located at the Fermi level, which is very robust against external biaxial and uniaxial strains. Treating the PC_5 monolayer as graphene with doped P atoms along the armchair direction, a 3*N* rule is found similar to that of graphene nanoribbons with armchair edges. These physical properties make the PC_5 monolayer a promising 2D material for emerging electronics applications.

1. Introduction

Since graphene was discovered by mechanical cleavage,[1,2] the Dirac cone materials, which show a linear band dispersion near the Fermi level, have been investigated intensively because of their novel physical properties and potential applications in nanoscale devices.[3,4] In particular, the massless fermions of the Dirac cone[4] lead to half-integer[2,5,6]/fractional[7]/fractal[8] quantum Hall effects (QHEs), ultrahigh carrier mobility,[9] and many other phenomena. The great development also motivates the continuous search for new Dirac cone materials. From 2D graphene to the 3D topological systems,[10–15] for example, the coexistence of Dirac points and Weyl points in momentum space can be realized in a hexagonal lattice SrHgPb.[15] Furthermore, in the 1D system, multiple Dirac points can also be revealed in the armchair single-wall carbon nanotube.[16]

As for the 2D system, much effort has been made to explore theoretically new carbon allotropes,[17–25] other elemental allotropes,[26–29] organometallic crystals,[30,31] sulfides,[32,33] carbides,[34–39] and so on. Even so, compared to the amount of 2D materials, large seeking for new 2D Dirac cone materials is still challenging work.[40]

It is known that both carbon and phosphorus form stable 2D monolayers and have similar structures including the threefold coordinated atoms and a hexagonal lattice,[4,41,42] so it is reasonable to assume that compound phosphorus carbide (PC) monolayer materials might exsit. Several 2D-monolayer PCs have been theoretically predicted to be stable,[42,43] and few-layer 2D black PC has been fabricated successfully in experiment through a new carbon doping technique.[44] These PC materials may have many excellent properties, for example, infrared phototransistors with a wide absorption spectrum made by few-layer black PC exhibit good responsivity and a minimum response time performance.[45] γ-PC and β_0-PC were proposed as alkali-metal-ion battery materials.[46,47] In our previous work, we have also predicted β_0-PC to be an intrinsic phonon-mediated superconductor, with an estimated superconducting temperature T_c of ≈13 K.[48]

Recently, a new 2D family of PC_x ($x = 2, 3, 5, 6$) was theoretically predicted by extensive structural search.[49] The PC_2 monolayer and PC_5 monolayer are metals, whereas the PC_3 monolayer and PC_6 monolayer are semiconductors. The PC_6 monolayer is predicted to be an excellent anode candidate[50–52] and a potential candidate as NO_x sensors.[53] The PC_3 monolayer is expected to be a high-capacity and rapidly charging anode material for sodium-ion batteries,[54] a promising photocatalyst for overall water splitting,[55] and thermoelectric material.[56] The PC_5 monolayer is expected to be a promising anode material for

L. Shang, Dr. H. Gao, Prof. W. Wu, Dr. Y. Wang, Prof. W. Ren
Department of Physics
International Center of Quantum and Molecular Structures
Shanghai University
Shanghai 200444, China
E-mail: renwei@shu.edu.cn

L. Shang, Dr. P.-F. Liu, Prof. B.-T. Wang
Institute of High Energy Physics
Chinese Academy of Sciences (CAS)
Beijing 100049, China
E-mail: wangbt@ihep.ac.cn

L. Shang, Dr. P.-F. Liu, Prof. B.-T. Wang
Spallation Neutron Source Science Center (SNSSC)
Dongguan 523803, China

Dr. Z. Gao
State Key Laboratory for Mechanical Behavior of Materials
Xi'an Jiaotong University
Xi'an 710049, China

Prof. B.-T. Wang
Collaborative Innovation Center of Extreme Optics
Shanxi University
Taiyuan 030006, China

The ORCID identification number(s) for the author(s) of this article can be found under https://doi.org/10.1002/pssr.202100203.

DOI: 10.1002/pssr.202100203

lithium-ion batteries.[52] In this PC family, the PC_2 monolayer and PC_5 monolayer possess a Dirac cone at the Fermi level.

Here, based on density functional theory (DFT), we systematically investigate the electronic properties of the PC_5 monolayer. Our calculations reveal that the PC_5 monolayer possesses a Dirac cone derived from C p_z orbitals with an ultrahigh Fermi velocity. The PC_5 monolayer can be treated as a doped graphene system with P atoms along the armchair direction. By changing the number of C_6 rings between P chains, we obtain the band structure of these monolayers and summarize a $3N$ rule.

2. Results and Discussion

2.1. Geometrical Properties

The hexagonal structure is the most favorable for the existence of Dirac cones[40] in the PC_5 monolayer material. Monolayer PC_5 has an anisotropic rectangular structure with lattice constants $a_1 = 4.39$ Å and $a_2 = 7.85$ Å. All the atoms in the unit cell of PC_5 are threefold coordinated, similar to the planar honeycomb lattice of graphene. The P atoms are aligned in a direction (armchair edge) and each P atom is coordinated with two C atoms, as shown in **Figure 1**a. The structure can be seen as the ribbons of C_6 rings separated between the P chains.

As shown in Figure 1a, the PC_5 monolayer possesses a buckled structure, which mainly stems from competition between the favored planar sp^2 hybridization of C atoms and the nonplanar sp^3 hybridization by P atoms. Each C bonds with the three nearest neighbors in a nearly planar configuration such that the C atoms are sp^2 hybridized. In contrast, the buckled configuration is shown near P atoms, implying sp^3 hybridization due to P atoms. This bonding configuration satisfies the chemical octet rule on both C and P sites and enhances the structural stability of the PC_5 monolayer.

The buckling thickness of the PC_5 monolayer, simply measured by the distance between the top and bottom atomic layers, is $d = 1.55$ Å, being slightly larger than that (1.24 Å) in the honeycomb lattice of semiconducting blue phosphorene.[57] Our calculated P—C bond length of monolayer PC_5 is 1.82 Å, which is larger than the P—C double bond length (1.67 Å) but nearly equal to the P—C single bond length (1.83 Å).[58,59]

2.2. Structural Stability

Stability is crucial for low-dimensional materials for their actual applications as electronic devices. To evaluate the stability of the PC_5 monolayer, we compute the formation energy with respect to the phosphorene[41,60] and graphene, defined as

$$E_f = \frac{E_{2D} - n_P E_P - n_C E_C}{n_P + n_C} \quad (1)$$

where E_{2D} is the total energy of the PC_5 monolayer, E_P and E_C are the energies of phosphorene and graphene per atom, and n_P and n_C are the number of P atoms and C atoms of the PC_5 monolayer, respectively. The result shows that the PC_5 monolayer has a formation energy of 0.28 eV per atom, which is slightly smaller than those we calculated of α-PC[42] (0.42 eV per atom) and β_0-PC[43] (0.66 eV per atom) monolayers. The similar positive formation energies suggest that PC_5, α-PC, and β_0-PC are equally stable. Although the synthesis of PC_5 may be an endothermic process, a small value means that PC_5 is not necessarily impossible to be synthesized. For example, the successful synthesis of metastable structures is already reported, such as the layered $As_{1-x}P_x$ compounds, which were predicted[61] and synthesized.[62] To examine the structural stability of PC_5, we further calculate the phonon dispersion spectrum and 2D elastic constants and perform ab initio molecular dynamics (AIMD) simulations. The results indicate that the PC_5 monolayer is dynamically, mechanically, and thermally stable. The phonon dispersion spectrum calculation is performed using a $3 \times 2 \times 1$ supercell and the result is shown in Figure 1b. As there are no imaginary frequencies, the PC_5 monolayer turns out to be dynamically stable. Based on the strain versus energy method, we extract the 2D elastic constants of the PC_5 monolayer. The C_{11}, C_{12}, C_{22}, and C_{66} are calculated to be 199.1, 22.3, 173.4, and 24.6 N m^{-1}, respectively. For the rectangular lattice, the Born criteria ($C_{11} > 0$, $C_{66} > 0$, $C_{11} \times C_{22} > C_{12} \times C_{12}$)[63] are satisfied in this structure, so the results suggest that this 2D structure is mechanically stable. Finally, we check the thermal stability of the PC_5 monolayer by conducting AIMD simulations. A large $3 \times 3 \times 1$ supercell under the temperature of 500 K is used during the simulations. After heating for 5 ps, the PC_5 monolayer does not have drastic structural distortions, and after

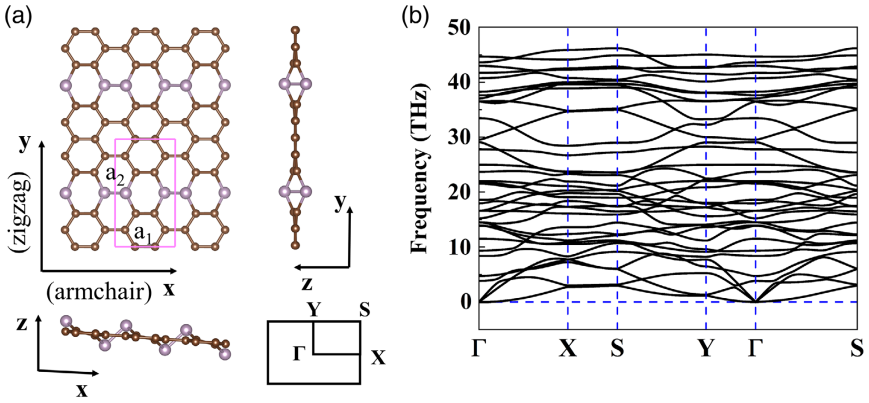

Figure 1. a) The structural geometry, including top view, side view, and the Brillouin zone of the PC_5 monolayer. a_1 and a_2 are the lattice constants. The small balls are C atoms and the large balls are P atoms. b) The phonon dispersions along the high-symmetry directions in the 2D Brillouin zone.

another optimization, the distorted monolayer structure can be restored to the initial structure. We can conclude that the PC_5 monolayer structure is thermally stable. These results of stability evaluation are consistent with the previous DFT work.[52]

2.3. Electronic Properties

The orbital-resolved band structure of the PC_5 monolayer is shown in **Figure 2**a. Here, we can see that the PC_5 monolayer shows a linear band-crossing point along the Γ–Y direction, which reveals its intrinsic metallicity, indicating good electronic conductivity. The merging point of the conduction band minimum (CBM) and the valence band maximum (VBM) is located at the (0, 0.24, 0) point in the reciprocal space and constitutes the Dirac cone exactly at the Fermi level, which is set to 0 eV. The Dirac cone is mainly originated from the p_z orbital of C atoms, which is similar to that in graphene (dominated by the p_z orbital). The s, p_x, and p_y orbitals of the C atom and s and p orbitals of the P atom mainly contribute to the deeper energy levels and hardly participate in the formation of the Dirac cone. The 3D valence and conduction bands are also calculated and shown in Figure 2b, which clearly show the features of the Dirac cone in the first Brillouin zone. There are two Dirac cones along the (010) direction. Furthermore, the existence of the Dirac cone has also been examined by the HSE06 calculation.

To obtain the bonding characters and electronic properties in the PC_5 monolayer, the electron localization function (ELF) and the partial charge densities at the Dirac points are calculated, as shown in **Figure 3**. The blue region is typical of a low-electron-density area, which indicates an ionic bond, whereas the region with an ELF value larger than 0.5 corresponds to a covalent bond or core electrons. The value of the ELF close to 0.5 means a metallic bond.[64,65] The ELF for the PC_5 monolayer shows that there are high-electron-localization regions between two adjacent carbon atoms. In other words, the electrons are mainly localized at the strong C—C bonding regions. The regions between P atoms and C atoms are also in the same situation. The analysis of the ELF clearly shows that the bonds between nearest-neighbor C atoms or P and C atoms are covalent. In the vicinity of P atoms, there are also high-electron-localization regions, which means the presence of lone-pair electrons of P atoms. Together with the buckled configuration near the P atoms, it further confirms that P atoms adopt an sp^3 hybridization.

In the real space, the partial charge densities of the CBM and VBM are originated from the four nearest C atoms to P chains (see Figure 3). The charge density distribution is derived from the out-of-plane (p_z orbital) states. The results clearly confirm that the couplings of C p_z orbitals along x and y directions, as shown in Figure 3c,d, cross each other and form the Dirac point.

The Dirac-cone-like electronic structures generally show excellent electronic transport properties due to the linear band character in the vicinity of the Dirac point. The Fermi velocity (v_f) values are calculated using the formula $v_f = (1/\hbar)(\partial E/\partial k)$, where $\partial E/\partial k$ is the slope of the valence or conduction band near the Dirac point and $\hbar$ is the reduced Planck's constant. The calculated v_f values of the PC_5 monolayer along $\Gamma \rightarrow Y$ and $Y \rightarrow \Gamma$ directions are 3.95×10^5 and -2.72×10^5 m s^{-1}, respectively, which are of the same order as that of graphene (9.5×10^5 m s^{-1}[66]). To verify our computational results of PC_5, we further calculate the Fermi velocity of graphene at the same theoretical level. The results are 9.44×10^5 and -9.33×10^5 m s^{-1} along $\Gamma \rightarrow K$ and $K \rightarrow \Gamma$ directions, respectively, which is consistent with the previous calculation result at the DFT level.[66] The linear dispersion curves of energy around the Dirac point suggest electron effective mass is zero near the Fermi level. The high Fermi velocity and massless carrier character in the PC_5 monolayer will benefit future electronics devices.

To further examine the robustness of the Dirac cones in the PC_5 monolayer, the different planar strains are applied on the monolayer by changing the lattice as $\epsilon = (a - a_0)/a_0$, where a_0 is the equilibrium lattice constant. It is found that the Dirac cones are robust to strain and can be well preserved within the biaxial strain range of −5% to 8%, as shown in **Figures 4** and **5**. When the external strain is larger than 8%, the VBM and CBM separate from each other and the Dirac cone is no longer present. It can be seen that the in-plane strain does not affect the contribution of the out-of-plane p_z (red) orbitals for the Dirac cone. As the tensile strain changes, the band from Y to Γ becomes flat, which means that the Dirac cone gradually becomes anisotropic. Then we apply the uniaxial strain, for example, the strain along the x-axis and y-axis directions, respectively, and show the results in **Figures 6** and **7**. As shown, the Dirac cone still survives under x-axis uniaxial strain in the range from

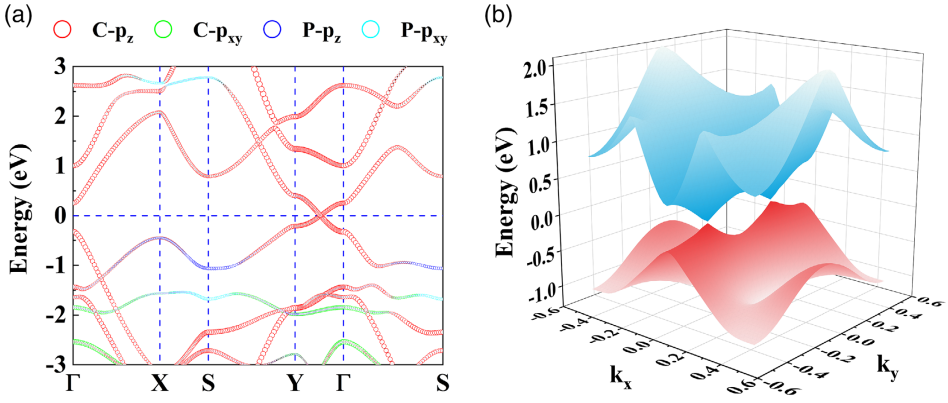

Figure 2. a) The orbital-resolved band structures of the PC_5 monolayer and b) the 3D band structures in the first Brillouin zone.

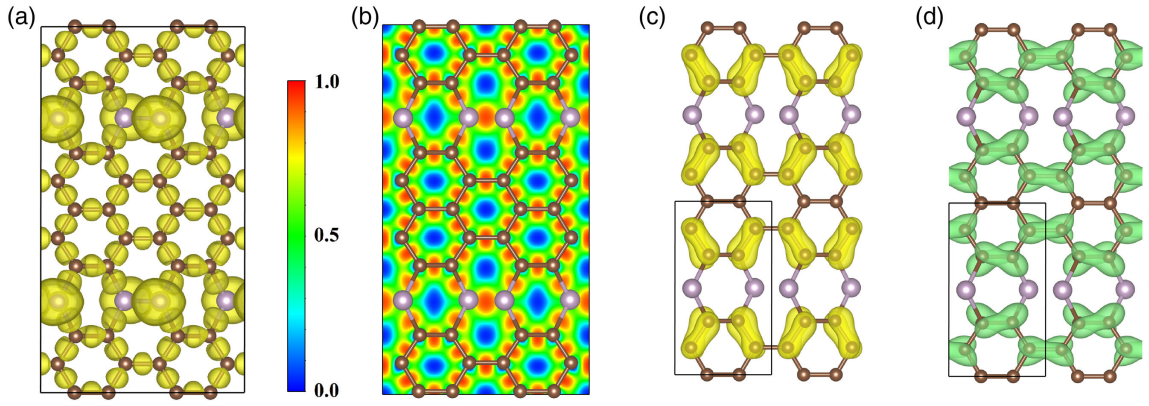

Figure 3. a) The ELF of the PC_5 monolayer with an isovalue of 0.7 au. b) ELF maps sliced perpendicular to the out-of-plane direction for the PC_5 monolayer. c) VBM and d) CBM charge density contours at the Dirac point.

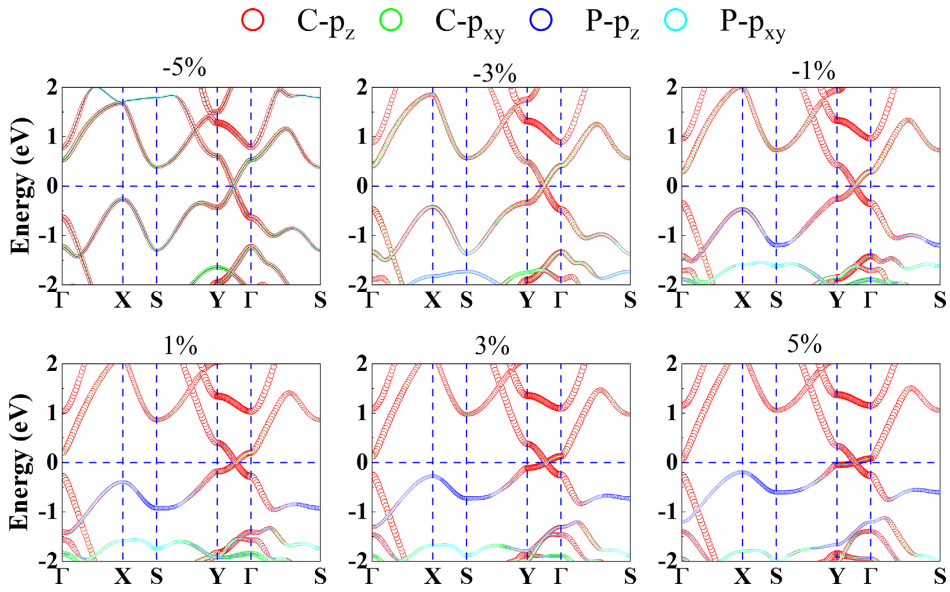

Figure 4. The orbital-resolved band structures of the PC_5 monolayer under biaxial strains from −5% to 5%.

−5% to 5%. The band structures of the PC_5 monolayer with different uniaxial strains along the *x*-axis are shown in Figure 6. When we apply the strain along the *y*-axis, we find that the Dirac point moves along the Y to Γ direction gradually, and when applying 5% tensile strain, the Dirac point is eventually located at the Γ point, as shown in Figure 7.

The partial charge densities of the VBM distribute along the *y*-axis direction, whereas the partial charge densities of the CBM distribute crossly along the *x*-axis direction. This can explain why the Dirac point is easily affected by the uniaxial strain along the *y*-axis. This insensitivity to the planar biaxial strain may be advantageous to its possible application in more complicated mechanical environments.

We also check the dynamic stability of the strained PC_5 monolayers. From our calculated phonon spectra under different strains (not shown), we find that when applying compressing strains, there are small imaginary frequencies in the acoustic phonon modes, whereas the tensile strains (up to 8%) never induce such dynamic instability. Although there are imaginary frequencies for compressed PC5 monolayers, we still want to investigate their electronic properties. Such unstable phonon modes may be stabilized by proper doping or substrate.

The Fermi velocities under different stains are also calculated and are shown in **Table 1**. We can see that the Fermi velocities decrease with increasing strain ϵ for both biaxial and uniaxial strain. This is due to a reduction of the overlap of the π-orbitals.[67] In addition, the $v_{x-\Gamma Y}$ and $v_{x-\Gamma Y}$ decrease slowly, whereas the $v_{y-\Gamma Y}$ and $v_{y-\Gamma Y}$ decrease rapidly. This result agrees well with the situation in graphene.[67] When applying the uniaxial strains in graphene, the Fermi velocity decreases along the strain axis and remains almost the same in the perpendicular direction.[67]

As mentioned previously, the distinguishing feature of the PC_5 monolayer is the alternation between P chains and the two C_6 rings. In other words, the PC_5 monolayer can be seen as graphene with doped P atoms along the armchair direction. So there is another thought that we change the number of the

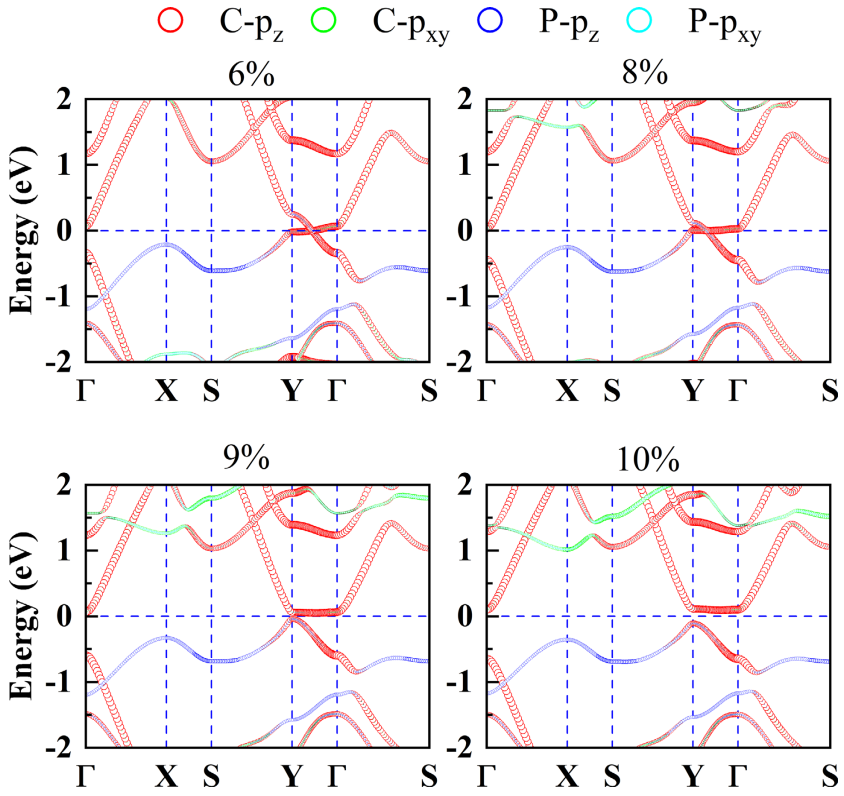

Figure 5. The orbital-resolved band structures of the PC_5 monolayer under biaxial strains from 6% to 10%.

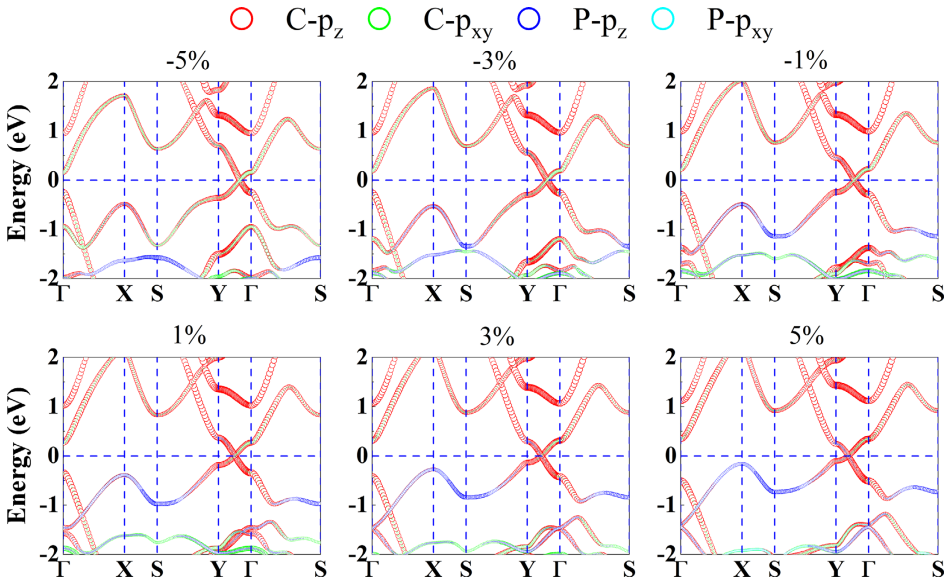

Figure 6. The orbital-resolved band structures of the PC_5 monolayer under uniaxial strains along the *x*-axis from −5% to 5%.

C_6 rings between P chains to see how the electronic structures of these monolayers change. We calculate the band structures of these monolayers with different numbers (from 1 to 9) of C_6 rings between P chains. We find that the band structures are similar among 1, 4, and 7 (2, 5, and 8; 3, 6, and 9) C_6 rings, as shown in **Figure 8**. It seems that there exists a rule that the band structures are similar with a multiple of 3 C_6 rings. As shown in Figure 8, the Dirac point is preserved when the structure has $3N-1$ C_6 rings between P chains. The VBM and CBM of $3N+1$ are located at the Γ point (except for 1), whereas the VBM and CBM of $3N$ systems are located at the Y point. The gap values of the $3N$ and $3N+1$ system are dependent

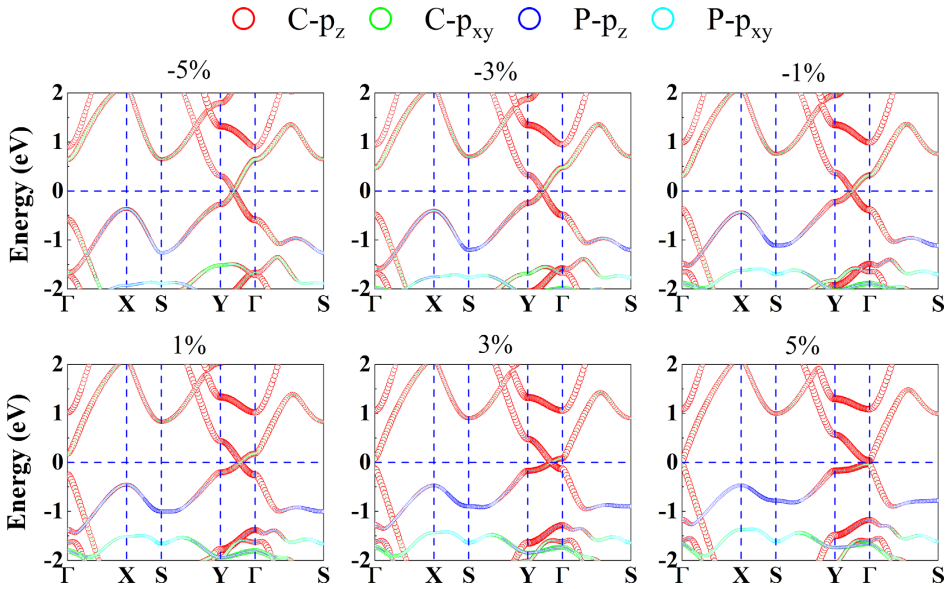

Figure 7. The orbital-resolved band structures of the PC_5 monolayer under uniaxial strains along the *y*-axis from −5% to 5%.

Table 1. The Fermi velocities (in the unit of $\times 10^5 m\,s^{-1}$) of different strained structures. $v_{b-\Gamma Y}$ and $v_{b-Y\Gamma}$ stand for the Fermi velocities under biaxial strains along the $\Gamma \to Y$ and $Y \to \Gamma$ directions, respectively. $v_{x-Y\Gamma}/v_{y-Y\Gamma}$ and $v_{x-\Gamma Y}/v_{y-\Gamma Y}$ represent the Fermi velocities under *x*/*y* uniaxial strains along the $\Gamma \to Y$ and $Y \to \Gamma$ directions, respectively.

Strain [%]	$v_{b-\Gamma Y}$	$v_{b-Y\Gamma}$	$v_{x-\Gamma Y}$	$v_{x-Y\Gamma}$	$v_{y-\Gamma Y}$	$v_{y-Y\Gamma}$
−5	5.99	4.76	4.51	2.86	4.51	4.35
−3	4.99	3.99	4.16	2.80	4.36	3.66
−1	4.23	3.10	4.02	2.76	4.13	3.01
1	3.73	2.26	3.93	2.57	3.70	2.31
3	3.53	1.47	3.90	2.32	2.91	1.52
5	3.50	0.76	3.88	2.06	2.20	0.84
6	3.45	0.41	–	–	–	–
8	2.77	0.06	–	–	–	–

on the widths between P chains (except for 1); that is, the gap values decrease as the widths increase. We conclude that the system is metallic when $M = 3N - 1$, where M is the number of C_6 rings between P atom chains, whereas the system is insulating when $M = 3N$ or $M = 3N + 1$.

There are other similar $3N$ rules found when carbon atoms are assembled into hexagonal lattices.[68–72]. For instance, after the dopant atoms N, B, S, Al, Si, and P are periodically doped in graphenes, there is a zero gap or a neglectable gap at the Dirac point when its primitive cell is $3N \times 3N$ (N is an integer).[68] Doping along the linear direction in graphenes has been studied in previous works;[69,73,74] there is a $3N$ rule found in the nitrogen-molecule-doped graphene system.[69] When $W = 3N - 1$ and $3N$ (N is an integer), the structures have type-I Dirac cones around the Fermi level, while they have type-II Dirac cones when $W = 3N + 1$. The structures in these linear doping systems contain pentagonal, hexagonal, and octagonal rings, whereas the structure in our work only has hexagonal rings. The graphene nanoribbons with armchair-shaped edges on both sides (AGNR) are metallic and show Dirac cone characteristics only when $M = 3N - 1$ (M denotes the number of dimer lines for armchair ribbons); otherwise AGNRs are insulating, and their bandgaps decrease with increasing N.[70,71] Other groups also have a similar conclusion that the band structure of AGNRs is metallic, displaying a Dirac point when the width in lattice constant units has the form $3N + 1$, with N an integer, and insulating otherwise.[72] The band structures of the two works described previously are modeled by a tight-binding approximation based on π electronic states and a 2D free massless particle Dirac's equation, respectively. However, based on first-principles approach, AGNRs are shown to have bandgaps, regardless of the width.[75] The edge effects, in which the bonds and the on-site energies of the carbons at the edges are different from those in the middle of the AGNRs, play a crucial role. These simplified models ignore the edge effect, so the neighbor hopping t is always the same and there is no change according to the location.

Our discovery is very similar to the $3N$ rule in AGNRs. The P-doped graphene and AGNR systems are very similar, where P chains can also be seen as the passivated atoms, just like hydrogen atoms at AGNR edges. Following the previous work,[71] the AGNRs are classified by the number of dimer lines across the ribbon width. The systems we calculated can be denoted as 3, 5, 7, 9, 11, 13, 15, 17, and 19, successively. The 5, 11, and 17 ($3N - 1$, N is the even integer) systems exactly follow the rule found in the aforementioned work. The energy gap decreases as the width increases, which is consistent with the results of the previous work. P atoms act as the armchair edges and ensure periodicity and continuity. Importantly, the band structures of $3N - 1$ show the Dirac cone characteristics from the first-principles calculation.

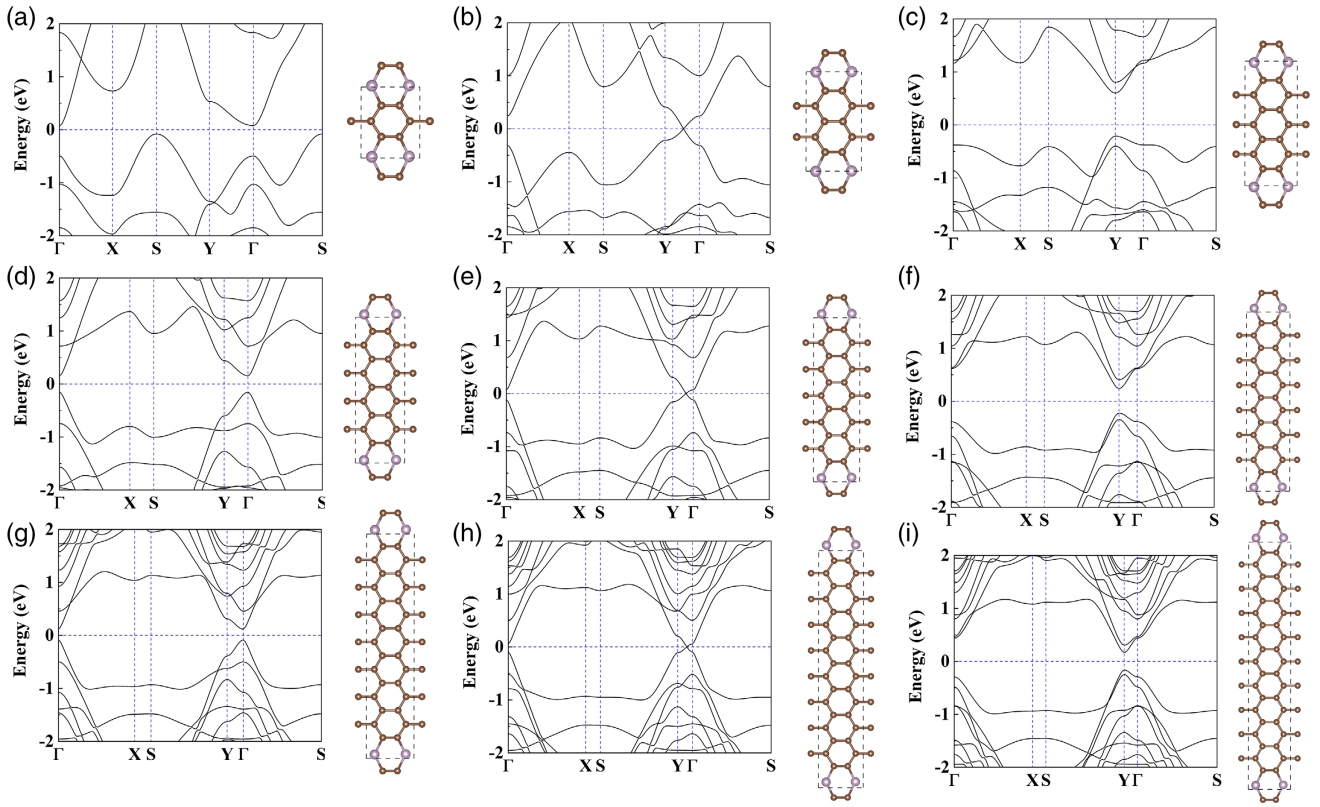

Figure 8. a–i) Electronic band structure and geometry structures of the monolayers with different numbers (1, 2, 3, 4, 5, 6, 7, 8, and 9) of C_6 rings between P chains, where b) is the PC_5 monolayer.

3. Conclusion

We have studied the PC_5 monolayer as a new family of 2D materials with intrinsic Dirac cone structure based on first-principles calculations. This monolayer, which is very similar to graphene with a hexagonal lattice, can be seen as doped graphene with P atoms along the armchair direction. The Dirac cone mainly originates from the contribution of C p_z orbitals. More importantly, it has a high Fermi velocity of the same order as graphene. Our results show that the PC_5 monolayer owns a robust Dirac cone structure against external biaxial strain in the range of −5% to 8%. In addition, we find a simple rule that the monolayers of $3N - 1$ C_6 rings between P chains show Dirac cone characteristics. The fascinating electronic properties make the PC_5 monolayer a promising 2D material for a future electronic application.

4. Experimental Section

The DFT calculations were performed using the Vienna Ab initio Simulation Package (VASP).[76] The Perdew–Burke–Ernzerhof (PBE)[77] form of the generalized gradient approximation (GGA)[78] was chosen as the exchange-correlation functional, and the van der Waals interaction was described by the DFT-D2 with Grimme correlation.[79] A vacuum space of about 19 Å perpendicular to the 2D plane was applied to avoid the artificially introduced interaction between the layers. The $3s^2 3p^3$ and $2s^2 2p^2$ atomic orbitals were treated as valence states for the P and C atoms, respectively. The geometry structures were fully relaxed until the residual force on each atom was less than 0.001 eV $Å^{-1}$. The property calculations were performed with plane-wave basis sets of 700 eV on the $12 \times 8 \times 1$ Monkhorst–Pack k-point mesh. The VASP raw data analysis was performed using VASPKIT.[80] The dynamic stability of the structure was examined by the Phonopy code.[81] Phonon dispersion spectra were calculated through the finite displacement method. AIMD simulation was conducted to confirm the thermal stability of the structure.

Acknowledgements

This work was supported by the National Natural Science Foundation of China (51861145315, 11929401, 12074241, 12074381, 11805214), the Independent Research and Development Project of State Key Laboratory of Advanced Special Steel, Shanghai Key Laboratory of Advanced Ferrometallurgy, Shanghai University (SKLASS 2020-Z07), the Science and Technology Commission of Shanghai Municipality (19DZ2270200, 19010500500, 20501130600), and the High Performance Computing Center, Shanghai University. The authors gratefully acknowledge financial support from the Ph.D. Start-up Fund of the Natural Science Foundation of Guangdong Province of China (Grant No. 2018A0303100013). The authors are also thankful for the computational resources from the Supercomputer Centre of the China Spallation Neutron Source.

Conflict of Interest

The authors declare no conflict of interest.

Data Availability Statement

The data that support the findings of this study are available from the corresponding author upon reasonable request.

Keywords

biaxial strain, Dirac cones, phosphorus carbides, 2D materials

Received: April 13, 2021
Revised: May 21, 2021
Published online:

[1] K. S. Novoselov, A. K. Geim, S. V. Morozov, D. Jiang, Y. Zhang, S. V. Dubonos, I. Grigorieva, A. A. Firsov, *Science* **2004**, *306*, 666.
[2] K. S. Novoselov, A. K. Geim, S. V. Morozov, D. Jiang, M. I. Katsnelson, I. V. Grigorieva, S. Dubonos, A. A. Firsov, *Nature* **2005**, *438*, 197.
[3] A. K. Geim, K. S. Novoselov, *Nat. Mater.* **2007**, *6*, 183.
[4] A. H. C. Neto, F. Guinea, N. M. R. Peres, K. S. Novoselov, A. K. Geim, *Rev. Modern Phys.* **2009**, *81*, 109.
[5] Y. Zhang, Y.-W. Tan, H. L. Stormer, P. Kim, *Nature* **2005**, *438*, 201.
[6] X. Du, I. Skachko, F. Duerr, A. Luican, E. Y. Andrei, *Nature* **2009**, *462*, 192.
[7] K. I. Bolotin, F. Ghahari, M. D. Shulman, H. L. Stormer, P. Kim, *Nature* **2009**, *462*, 196.
[8] C. R. Dean, L. Wang, P. Maher, C. Forsythe, F. Ghahari, Y. Gao, J. Katoch, M. Ishigami, P. Moon, M. Koshino, T. Taniguchi, K. Watanabe, K. L. Shepard, J. Hone, P. Kim, *Nature* **2013**, *497*, 598.
[9] K. I. Bolotin, K. J. Sikes, Z. Jiang, M. Klima, G. Fudenberg, J. Hone, P. Kim, H. L. Stormer, *Solid State Commun.* **2008**, *146*, 351.
[10] S. M. Young, S. Zaheer, J. C. Y. Teo, C. L. Kane, E. J. Mele, A. M. Rappe, *Phys. Rev. Lett.* **2012**, *108*, 140405.
[11] Z. K. Liu, B. Zhou, Y. Zhang, Z. J. Wang, H. M. Weng, D. Prabhakaran, S.-K. Mo, Z. X. Shen, Z. Fang, X. Dai, Z. Hussain, Y. L. Chen, *Science* **2014**, *343*, 864.
[12] Z. K. Liu, J. Jiang, B. Zhou, Z. J. Wang, Y. Zhang, H. M. Weng, D. Prabhakaran, S.-K. Mo, H. Peng, P. Dudin, T. Kim, M. Hoesch, Z. Fang, X. Dai, Z. X. Shen, D. L. Feng, Z. Hussain, Y. L. Chen, *Nat. Mater.* **2014**, *13*, 677.
[13] J. A. Steinberg, S. M. Young, S. Zaheer, C. L. Kane, E. J. Mele, A. M. Rappe, *Phys. Rev. Lett.* **2014**, *112*, 036403.
[14] W. Zhou, H. Gao, J. Zhang, R. Fang, H. Song, T. Hu, A. Stroppa, L. Li, X. Wang, S. Ruan, W. Ren, *Phys. Rev. B* **2017**, *96*, 064103.
[15] H. Gao, Y. Kim, J. W. F. Venderbos, C. L. Kane, E. J. Mele, A. M. Rappe, W. Ren, *Phys. Rev. Lett.* **2018**, *121*, 106404.
[16] W. Ren, T. H. Cho, T. C. Leung, C. T. Chan, *Appl. Phys. Lett.* **2008**, *93*, 142102.
[17] D. Malko, C. Neiss, F. Vines, A. Görling, *Phys. Rev. Lett.* **2012**, *108*, 086804.
[18] Y. Liu, G. Wang, Q. Huang, L. Guo, X. Chen, *Phys. Rev. Lett.* **2012**, *108*, 225505.
[19] H. Huang, W. Duan, Z. Liu, *New J. Phys.* **2013**, *15*, 023004.
[20] M. Zhao, W. Dong, A. Wang, *Sci. Rep.* **2013**, *3*, 3532.
[21] L.-C. Xu, R.-Z. Wang, M.-S. Miao, X.-L. Wei, Y.-P. Chen, H. Yan, W.-M. Lau, L.-M. Liu, Y.-M. Ma, *Nanoscale* **2014**, *6*, 1113.
[22] Z. Wang, X.-F. Zhou, X. Zhang, Q. Zhu, H. Dong, M. Zhao, A. R. Oganov, *Nano Lett.* **2015**, *15*, 6182.
[23] L. Z. Zhang, Z. F. Wang, Z. M. Wang, S. X. Du, H.-J. Gao, F. Liu, *J. Phys. Chem. Lett.* **2015**, *6*, 2959.
[24] X. Zhang, L. Wei, J. Tan, M. Zhao, *Carbon* **2016**, *105*, 323.
[25] H. Gao, W. Ren, *Carbon* **2020**, *158*, 210.
[26] S. Cahangirov, M. Topsakal, E. Aktürk, H. Sahin, S. Ciraci, *Phys. Rev. Lett.* **2009**, *102*, 236804.
[27] C. Liu, T. Hu, Y. Wu, H. Gao, Y. Yang, W. Ren, *J. Phys. Condens. Matter* **2019**, *31*, 235702.
[28] R.-W. Zhang, C.-W. Zhang, W.-X. Ji, S.-S. Li, S.-J. Hu, S.-S. Yan, P. Li, P.-J. Wang, F. Li, *New J. Phys.* **2015**, *17*, 083036.
[29] X.-F. Zhou, X. Dong, A. R. Oganov, Q. Zhu, Y. Tian, H.-T. Wang, *Phys. Rev. Lett.* **2014**, *112*, 085502.
[30] Z. F. Wang, Z. Liu, F. Liu, *Nat. Commun.* **2013**, *4*, 1.
[31] Z. F. Wang, Z. Liu, F. Liu, *Phys. Rev. Lett.* **2013**, *110*, 196801.
[32] W. Li, M. Guo, G. Zhang, Y.-W. Zhang, *Phys. Rev. B* **2014**, *89*, 205402.
[33] Y. Zhao, X. Li, J. Liu, C. Zhang, Q. Wang, *J. Phys. Chem. Lett.* **2018**, *9*, 1815.
[34] X. Qin, Y. Wu, Y. Liu, B. Chi, X. Li, Y. Wang, X. Zhao, *Sci. Rep.* **2017**, *7*, 1.
[35] C. Pu, D. Zhou, Y. Li, H. Liu, Z. Chen, Y. Wang, Y. Ma, *J. Phys. Chem. C* **2017**, *121*, 2669.
[36] B. Wang, S. Yuan, Y. Li, L. Shi, J. Wang, *Nanoscale* **2017**, *9*, 5577.
[37] P.-F. Liu, L. Zhou, S. Tretiak, L.-M. Wu, *J. Mater. Chem. C* **2017**, *5*, 9181.
[38] P.-F. Liu, Y. Wu, T. Bo, L. Hou, J. Xu, H.-J. Zhang, B.-T. Wang, *Phys. Chem. Chem. Phys.* **2018**, *20*, 732.
[39] L. Zhou, B. Shao, W. Shi, Y. Sun, C. Felser, B. Yan, T. Frauenheim, *2D Mater.* **2016**, *3*, 035022.
[40] J. Wang, S. Deng, Z. Liu, Z. Liu, *Nat. Sci. Rev.* **2015**, *2*, 22.
[41] H. Liu, A. T. Neal, Z. Zhu, Z. Luo, X. Xu, D. Tománek, P. D. Ye, *ACS Nano* **2014**, *8*, 4033 c.
[42] G. Wang, R. Pandey, S. P. Karna, *Nanoscale* **2016**, *8*, 8819.
[43] J. Guan, D. Liu, Z. Zhu, D. Tománek, *Nano Lett.* **2016**, *16*, 3247.
[44] W. C. Tan, Y. Cai, R. J. Ng, L. Huang, X. Feng, G. Zhang, Y.-W. Zhang, C. A. Nijhuis, X. Liu, K.-W. Ang, *Adv. Mater.* **2017**, *29*, 1700503.
[45] W. C. Tan, L. Huang, R. J. Ng, L. Wang, D. M. N. Hasan, T. J. Duffin, K. S. Kumar, C. A. Nijhuis, C. Lee, K.-W. Ang, *Adv. Mater.* **2018**, *30*, 1705039.
[46] W. Zhang, J. Yin, P. Zhang, X. Tang, Y. Ding, *J. Mater. Chem. A* **2018**, *6*, 12029.
[47] F. Li, X. Liu, J. Wang, X. Zhang, B. Yang, Y. Qu, M. Zhao, *Electrochim. Acta* **2017**, *258*, 582.
[48] B.-T. Wang, P.-F. Liu, T. Bo, W. Yin, O. Eriksson, J. Zhao, F. Wang, *Phys. Chem. Chem. Phys.* **2018**, *20*, 12362.
[49] T. Yu, Z. Zhao, Y. Sun, A. Bergara, J. Lin, S. Zhang, H. Xu, L. Zhang, G. Yang, Y. Liu, *J. Am. Chem. Soc.* **2019**, *141*, 1599.
[50] K. Dou, Y. Ma, T. Zhang, B. Huang, Y. Dai, *Phys. Chem. Chem. Phys.* **2019**, *21*, 26212.
[51] J. Zhang, L. Xu, C. Yang, X. Zhang, L. Ma, M. Zhang, J. Lu, *Appl. Surf. Sci.* **2020**, *510*, 145493.
[52] K. Fan, Y. Ying, X. Luo, H. Huang, *Phys. Chem. Chem. Phys.* **2020**, *22*, 16665.
[53] X. Yu, L. Xiao, Y. Li, *Physica E* **2020**, *118*, 113958.
[54] S. Jana, S. Thomas, C. H. Lee, B. Jun, S. U. Lee, *Carbon* **2020**, *157*, 420.
[55] H. Yao, Q. Wang, J. Li, W. Cai, Y. Wei, B. Wang, J. Wang, *Phys. Chem. Chem. Phys.* **2020**, *22*, 9477.
[56] K. Rajput, D. R. Roy, *Phys. Chem. Chem. Phys.* **2020**, *22*, 8625.
[57] V. O. Özcelik, J. G. Azadani, C. Yang, S. J. Koester, T. Low, *Phys. Rev. B* **2016**, *94*, 035125.
[58] J. J. Daly, *J Chem. Soc.*, **1964**, *729*, 3799.
[59] B. Rajbanshi, P. Sarkar, *J. Phys. Chem. Lett.* **2017**, *8*, 747.
[60] L. Li, Y. Yu, G. J. Ye, Q. Ge, X. Ou, H. Wu, D. Feng, X. H. Chen, Y. Zhang, *Nat. Nanotechnol.* **2014**, *9*, 372.

[61] Z. Zhu, J. Guan, D. Tománek, *Nano Lett.* **2015**, *15*, 6042.
[62] B. Liu, M. Köpf, A. N. Abbas, X. Wang, Q. Guo, Y. Jia, F. Xia, R. Weihrich, F. Bachhuber, F. Pielnhofer, H. Wang, R. Dhall, S. B. Cronin, M. Ge, X. Fang, T. Nilges, C. Zhou, *Adv. Mater.* **2015**, *27*, 4423.
[63] M. Mazdziarz, *2D Mater.* **2019**, *6*, 048001.
[64] J. K. Burdett, T. A. McCormick, *J. Phys. Chem. A* **1998**, *102*, 6366.
[65] V. Tsirelson, A. Stash, *Chem. Phys. Lett.* **2002**, *351*, 142.
[66] P. E. Trevisanutto, C. Giorgetti, L. Reining, M. Ladisa, V. Olevano, *Phys. Rev. Lett.* **2008**, *101*, 226405.
[67] M. Huang, H. Yan, T. F. Heinz, J. Hone, *Nano Lett.* **2010**, *10*, 4074.
[68] Y.-C. Zhou, H.-L. Zhang, W.-Q. Deng, *Nanotechnology* **2013**, *24*, 225705.
[69] H. Zhang, Y. Xie, C. Zhong, Z. Zhang, Y. Chen, *J. Phys. Chem. C* **2017**, *121*, 12476.
[70] M. Fujita, K. Wakabayashi, K. Nakada, K. Kusakabe, *J. Phys. Soc. Jpn.***1996**, *65*, 1920.
[71] K. Nakada, M. Fujita, G. Dresselhaus, M. S. Dresselhaus, *Phys. Rev. B* **1996**, *54*, 17954.
[72] L. Brey, H. A. Fertig, *Phys. Rev. B* **2006**, *73*, 235411.
[73] Y. Li, R.-Q. Zhang, Z. Lin, M. A. Van Hove, *Appl. Phys. Lett.* **2012**, *101*, 253105.
[74] J.-C. Ren, Z. Ding, R.-Q. Zhang, M. A. Van Hove, *Phys. Rev. B* **2015**, *91*, 045425.
[75] Y.-W. Son, M. L. Cohen, S. G. Louie, *Phys. Rev. Lett.* **2006**, *97*, 216803.
[76] G. Kresse, J. Furthmüller, *Phys. Rev. B* **1996**, *54*, 11169.
[77] J. Paier, R. Hirschl, M. Marsman, G. Kresse, *J. Chem. Phys.* **2005**, *122*, 234102.
[78] J. P. Perdew, K. Burke, M. Ernzerhof, *Phys. Rev. Lett.* **1996**, *77*, 3865.
[79] S. Grimme, *J. Comput. Chem.* **2006**, *27*, 1787.
[80] V. Wang, N. Xu, J.-C. Liu, G. Tang, W.-T. Geng, *Comput. Phys. Commun.* **2019**, *267*, 108033.
[81] A. Togo, F. Oba, I. Tanaka, *Phys. Rev. B* **2008**, *78*, 134106.